Chapter 3

Role of density gradients in spherical plasma targets on the generation of fast proton beams

The work included in this chapter is published partly in A. Bhagawati and N. Das, "Laser-accelerated protons using density gradients in hydrogen plasma spheres." Journal of Plasma Physics, 87(4) (2021) and partly in A. Bhagawati, "Role of Laser Pre-pulse and Target Density Modification on the Acceleration of Protons from a Hydrogen Plasma Sphere" in Selected Progresses in Modern Physics (pp. 313-319). Springer, Singapore, (2021).

In all the available high-power laser facilities, the intense main-pulse is usually preceded by a pre-pulse of lower intensity which hits the target and ionizes it to form plasma. A finite time delay between the pre-pulse and the main pulse results in the plasma target to undergo expansion. The target density thus gets modified with a central peak density that gradually decreases nearly isotropically towards the edges. The effect of different density profiles on micron-sized hydrogen plasma spheres is investigated when the plasma gets irradiated with an ultra-short circularly polarized laser. In this study, we show that significant improvement in the characteristics of the accelerated protons viz maximum proton energy, as well as their mono-energetic behaviour, is possible by using a plasma sphere having a tailored density profile. A radial linear-shaped density distribution is introduced in the plasma sphere and the density gradient is tuned by changing the peak density at the centre. The optimum regime of

steepness is found for the maximum energy attained by the protons where the target is opaque enough for the radiation pressure to play its role, however not too opaque to inhibit efficient target heating. A novel Gaussian-shaped density profile is suggested which plays an important role in suppressing the sheath field. With a decreased rear side field, a visible improvement of the mono-energetic feature of the protons is observed.

3.1 Motivation and background of the study

The interaction of the intense laser pulse with a solid target results in the reflection of a significant amount of the laser energy from the target front-side. Therefore, the laser-to-electron energy conversion is rather low in such targets. This resulted in the quest for an engineered target that absorbs most of the laser energy which leads to the generation of hot electrons more efficiently in the vacuum-target interface. Several micro or nano-structured targets [1, 2, 3] have shown an improved absorption efficiency of the target leading to the formation of quasi-monoenergetic ion beams. The use of a critical density target with plasma density $n_e \sim n_c$, where $n_c = \dfrac{m_e\omega^2}{4\pi e^2}$ causes a significant amount of the laser energy to get absorbed in the plasma and effectively produces energetic electrons [4]. Here, ω is the laser frequency, and m_e and e are the electronic mass and charge respectively. As the laser propagation is inhibited around the critical density, it steepens the plasma profile and heats the electrons efficiently. The heated electrons perturb the background plasma and drive a return current. This fast return current plays an important role in heating the entire plasma volume.

It is found that a smooth density gradient at the front side of the target increases the laser absorption inside it [5, 6, 7, 8]. This is in contrast with homogeneous density targets, where the main laser pulse enters an over-dense regime instantly, and thus most of its energy is reflected. In almost all the available high-power laser facilities, the main laser pulse is preceded by a pre-pulse of lower intensity. This pre-pulse hits the solid

density foil target and ionizes it to form a plasma layer. The density of the target thus decreases due to the plasma expansion, and the main pulse encounters a smoothly increasing density profile instead of a sharp vacuum-solid interface. The plasma layer created due to the prepulse has a smooth density gradient both at the target front and the rear [9]. Moreover, a decreasing density gradient at the rear side of the target helps in maintaining the mono-energetic nature of the ejected ion bunches by the formation of an evenly distributed TNSA field [10, 11]. It has been observed that for the production of monoenergetic protons the characterizing density scale length (L) must be such that $\frac{4\pi c_s^2}{v_s \omega_{pi}} \ll L \leq \frac{\pi c}{\omega_{pi}}$ [12]. Here $\omega_{pi} = \sqrt{\frac{4\pi n e^2}{m_i}}$ is the ion-plasma frequency. A larger inhomogeneity scale length at the foil front increases the absorption coefficient, thereby increasing the temperature of fast electrons and the energy of accelerated ions [8]. The production of energetic ions thus depends significantly on the density gradient and scale length. A detailed simulation study using near-critical mass-limited spheres was reported in [13] where the targets were heated by a pre-pulse leading to the target expansion and reduction in the density in the target front side. They obtained an optimized parameter space for producing protons having tunable energies. The acceleration regime behind the energetic ions of mass m_i from different regions of the target usually depend on the target density and the delay time between the two pulses. The tailoring of the density profile can tune the inherent ion acceleration mechanisms. It has been shown using Eulerian Vlasov-Maxwell simulations that the final mono-energetic behaviour of the ions can be preserved with a target having a layered density structure [14]. Moreover it was found that the interaction of intense lasers with modified targets having soliton-like density profiles can be administered to obtain energetic protons of controllable beam properties [15]. A steep density gradient resulted in protons accelerating with higher energies via an interplay of RPA and TNSA mechanisms with a higher angle of divergence.

In this chapter, a study is made on the role of the pre-pulse strength and the eventual modification of the target properties on the acceleration

of the protons. We have performed 3D Particle in Cell (PIC) simulations to study the effects of different density inhomogeneities in a micron-sized spherical (droplet) target when irradiated with a femtosecond pulsed laser. The target diameter is kept less than the laser spot-size to ensure proper focusing of the laser on-to the target [6, 16, 17, 18]. In many practical situations, it is difficult to maintain a homogeneous density of the target as the presence of a prepulse and the pedestal of the main pulse tend to expand the plasma isotropically creating a gradually decreasing density profile starting with the target centre. In the simulation setup, the presence of the pre-pulse is taken into account by considering a pre-deformed plasma target. The prime objective of this chapter is to investigate the acceleration of protons from a plasma droplet having a tailored density profile such that its density is peaked at the centre and dropping gradually towards the edges. In a 2D3V PIC simulation work [6], a study is made on the effect of an exponential density profile in the front side of a solid mass-limited target on the absorption of the laser inside the target. They found enhanced hot electron temperature and density in presence of the pre-plasma. In a similar work [19], a linear and exponential density profile is implemented in the front and rear side of an expanded foil target to suppress the proton energy spread and obtain a distinct peak in the energy spectrum. However, in all the previous reported works, a comparison of different density gradients both at the front and rear sides of a microsphere plasma was missing to the best of our knowledge. Moreover, a radially Gaussian-shaped inhomogeneity is proposed in this work that supports a prominent monoenergetic peak in the proton spectra. Such a density profile is somewhat unexplored as far as our knowledge goes. To attain high quality and efficient hole boring RPA, a density-modified target was used in [20] which had a Gaussian type variation in the plasma density along the laser direction. With a peak $a_0 = 100$, a mean energy of 30 MeV is obtained from the monoenergetic beam of ions. Although a Gaussian-shaped density profile is proposed in our present work, its exact geometry is vastly different from the work in [20]. Due to the spherical shape of the target considered

in our simulations, our target has a radial Gaussian density variation and not just along the longitudinal direction. We have considered that the target is composed of pure hydrogen with only electrons and protons as the plasma constituents with proton mass $m_p = 1836m_e$. Thus, the terms "ions" and "protons" are interchangeable in this study. At first, the inhomogeneity is assumed to be linear in the first approximation. As the main pulse gradually travels from an underdense to an overdense plasma at the core of the target, several rich physical phenomena emerge which were not seen in previous studies. In contrast to Chapter 2 [21], where a uniform density target was used, the enhanced laser-to-plasma energy absorption, in this case, resulted in quasi-monoenergetic peaks in the proton spectrum. In this chapter, a comparison is made between the protons accelerated from an inhomogeneous target with that of a target of uniform density. It is found that the rear-side electrostatic field in an inhomogeneous target is reduced to quite an extent which results in the persistence of the mono-energetic feature of the protons for a longer time. The role of the peak density at the centre is analysed in the slightly overdense regime ensuring sufficient heating of the target by the energetic electrons. The role of radiation pressure is seen to be accentuated as the peak density (i.e. the density gradient) is increased, which can be predicted from previous literature. Further, when the inhomogeneity is shifted from being a linear one to a novel Gaussian profile, the proton energy spectra showed a more pronounced peak which resulted due to the combined effect of an enhanced RPA-HB effect on the protons in the front side and a suppressed TNSA field on the rear side.

3.2 Simulation model description

We have used Picpsi 3D [22], a relativistic 3 dimensional PIC code to study the interaction of high-intensity circularly polarized laser with an inhomogeneous density spherical plasma target. A laser pulse having both spatial and temporal Gaussian pulse profile with wavelength $1\mu m$ and laser period $3.3fs$ is allowed to propagate along the Z-axis. The

laser has a spatial FWHM (full width at half maxima) of $10\mu m$ and the laser pulse duration (temporal FWHM) $\tau_L = 33fs$. The critical density for $1\mu m$ laser is $n_c = 1.1 \times 10^{21} cm^{-3}$. Throughout this work, we have used a laser intensity $I_L = 1.37 \times 10^{20} W/cm^2$ corresponding to normalized vector potential $a_0 = \dfrac{eE_0}{\sqrt{2}m_e\omega c} \approx 7.07$. The relativistic intensity allows the laser to penetrate the normally over-dense target due to induced transparency. The simulation box used is a cube of length, $20\mu m$ with each side consisting of 400 cells. The target is transparent to the laser pulse up to a relativistically enhanced skin depth which exceeds the classical skin depth by a factor $\sqrt{\gamma}$. The relativistic intensity of the laser pulse thus helps in resolving the skin depth by the cell size. A pre-deformed spherical hydrogen plasma target is placed equidistant from all six sides of the simulation box. The centre of the plasma target coincides with the $10\mu m$ mark of the box and the space between the target and the walls consists of a vacuum. Absorbing boundary conditions for both the fields and the particles are used along all the six walls. All the simulations are performed with 50 macro-particles per cell and one time-step $T_0 = 0.2\omega_p^{-1}$, where ω_p is the plasma frequency corresponding to the peak density (n_{peak}) of the target.

3.3 Results and discussions

3.3.1 Effect of a secondary laser pulse/ pre-pulse

In the simulation set-up, the presence of the pre-pulse is taken into account by considering a pre-deformed plasma target. The hydrogen plasma target considered in the present work is a micron-sized sphere of solid density (density of solid hydrogen is $n_0 \simeq 6 \times 10^{22} cm^{-3} \simeq 53 n_c$). This density is, however, maintained for the main laser pulse only when the laser system is free of any pre-pulse. However, this is realistically almost never true. In presence of a pre-pulse of peak intensity ($\tilde{a_0} < a_0$), the target density get modified and a density gradient is formed. For a spherical plasma target (as in the present case), a sufficiently high inten-

sity prepulse will ionize the solid hydrogen target and create a density variation such that the density is peaked at the centre of the sphere and dropping gradually towards the periphery. The drop in density from the centre is considered to be isotropic for simplicity.

The pre-pulse intensity is directly correlated with the central peak density (n_{peak}) and the delay time (Δt) between the pre-pulse and the main pulse using [13]

$$\tilde{a_0} = 4.7 \times 10^{-3} \sqrt{\frac{m_i}{m_e}} (\sigma - 1) \frac{R_0[\mu m]}{\Delta t[ps]} \tag{3.1}$$

Here, $\sigma = \dfrac{R}{R_0} = \left(\dfrac{n_0}{n_{peak}}\right)^{1/3}$ such that the radius of the target increases from R_0 to R as the density drops when a pre-pulse of normalized vector potential $\tilde{a_0}$ hits upon it. For these simulations, the peak of the main pulse interaction occurs at $\approx 188fs$ which is assumed to be the time delay (Δt) between the pulses. By varying the pre-pulse intensity, therefore, the plasma target for the main pulse could be tuned to obtain the optimum accelerating condition of the protons. We varied $\tilde{a_0}$ from 0 to 2 by varying the values of the modified target radius and the central peak density as shown in Table 3.1.

Table 3.1: Variation of the prepulse strength with the modified target radius and the peak plasma density at the centre. The time delay between the pulses is $188fs$.

Pre-pulse strength, $\tilde{a_0}$	Radius, R $[\mu m]$	Peak density (n_{peak}/n_c)
0	1.5 (R_0)	53 (solid H)
0.1	1.59	45.1
0.5	1.97	24
0.8	2.25	16.08
0.9	2.34	14.24
1	2.5	12
1.2	2.62	10.14
1.5	3.11	6.08
2	3.37	4.78

Fig. 3.1 shows the maximum proton energy obtained for different values of $\tilde{a_0}$. It is seen that $\tilde{a_0} = 0.5$ is the optimal energy case with

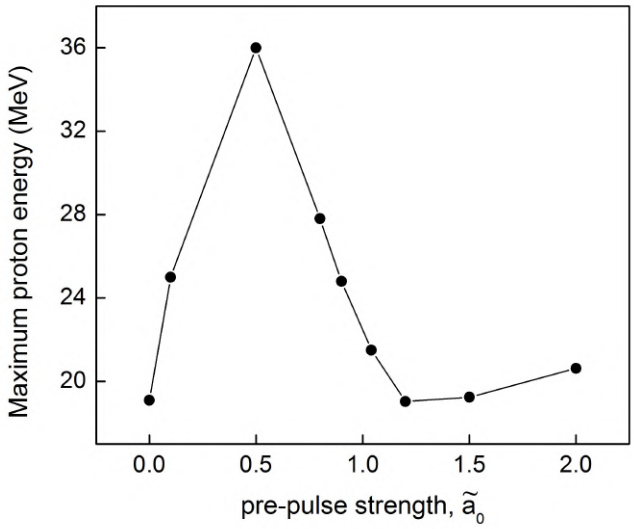

Figure 3.1: The variation of maximum proton energy with the pre-pulse strength $\tilde{a_0}$

maximum proton energy $\approx 36MeV$. It can be seen that the presence of the pre-pulse favours the generation of higher energetic protons when $\tilde{a_0} < 1$. Fig. 3.2 shows the longitudinal proton momentum for four different strengths of the pre-pulse at different times. These phase space plots give the information about the dominant acceleration mechanisms that are participating after the interaction with the main-pulse. It is seen that in the no pre-pulse ($\tilde{a_0} = 0$) case [Fig. 3.2(a)], most of the protons gain momentum from the front side of the target. The sharp vacuum-target interface faced by the main-pulse supports a strong density steepening at the front side of the target caused by the radiation pressure effect of the pulse. The laser propagation is stopped around the skin-depth and the plasma heating by the laser remains minimal. For the optimal energy case of $\tilde{a_0} = 0.5$ in Fig. 3.2(b), the formation of a shock is visible in the downward density gradient ($Z > 10\mu m$) of the target. The protons reflected from the shock front gives an additional push to the expanding background protons and is the reason behind the production of high energetic protons compared to the other cases. The shock formation is also seen in Fig. 3.2(c) for $\tilde{a_0} \simeq 1$. The maximum proton energy achieved in this case is however less in comparison the maximum energy obtained in

the case with $\tilde{a_0} = 0.5$. When the pre-pulse strength is further increased to 1.5, the drop in the central density n_{peak} to $6.08n_c$ makes the target transparent to the main laser pulse and plasma expansion becomes the dominant mechanism. This is visible in Fig. 3.2(d) where the phase space displays a fairly uniform expansion of the target in both the forward and backward directions. With a further increase in the pre-pulse strength beyond this case, the maximum proton energy seems to slightly increase as seen from Fig. 3.1. This is because of a stronger expansion of the target before the laser main-pulse hit upon it, rendering the target under-dense for the main-pulse. As a result, the protons gain energy and are exploded in an isotropic manner.

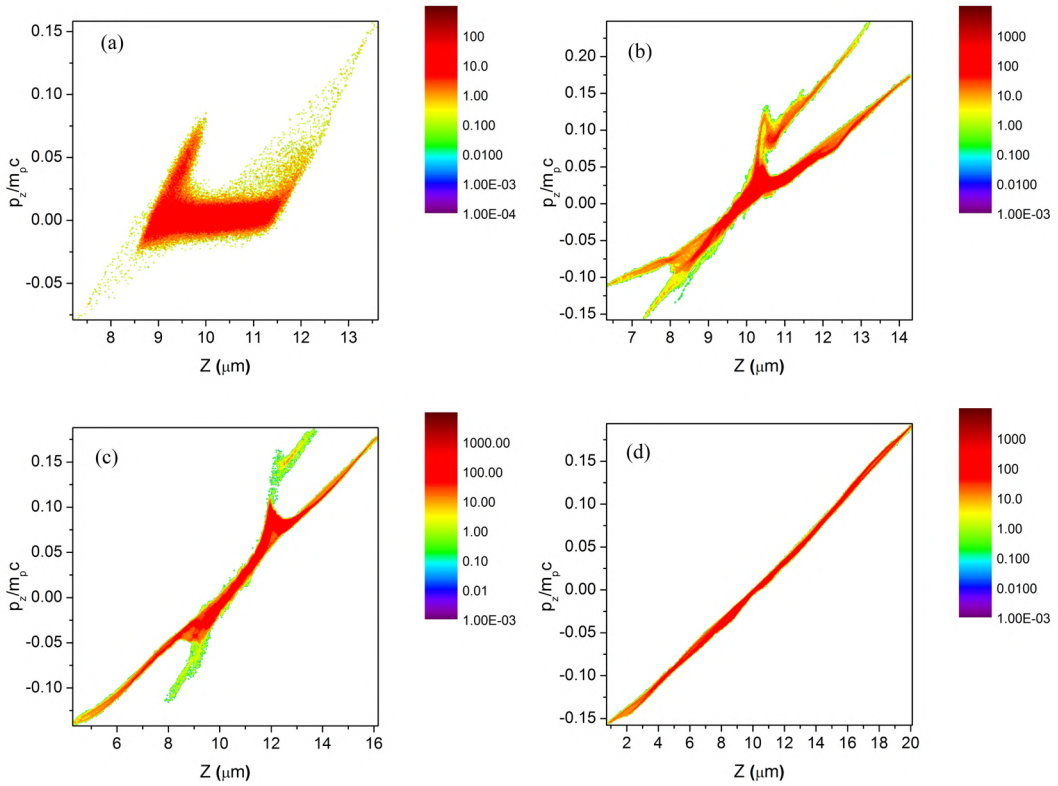

Figure 3.2: The longitudinal proton momenta (p_z) along Z at the proton saturation time for four different cases with (a)$\tilde{a_0} = 0$ i.e. no pre-pulse at 246 fs, (b) $\tilde{a_0} = 0.5$ at 271.2 fs, (c) $\tilde{a_0} \simeq 1$ at 307 fs, and (d) $\tilde{a_0} = 1.5$ at 388 fs. The colour axis represents the proton distribution in arbitrary units.

3.3.2 Radially linear target density distribution

To understand the effect of the density gradient we first introduce the laser pulse to a spherical plasma target having a linear density gradient, such that the density is peaked at the centre and linearly dropping towards the edges. The peak density (n_{peak}) is varied (starting with $8n_c$) so that the laser encounters an overdense region near the centre. The relativistically induced transparency renders the target dilute for the laser at the near-surface of the plasma target. The results in plasma expansion due to the pre-pulse interaction on a solid target can be modelled as a linear density gradient in the first approximation. As suggested in [19] the peak density is $n_{peak} = \dfrac{n_0 d_0}{2c_{s0}\Delta t}$, where $c_{s0} = \sqrt{\dfrac{T_e}{m_p}}$ is the ion-acoustic velocity after interaction with the pre-pulse and n_0 and d_0 are the original density and diameter of the solid hydrogen target, respectively. The expansion of the target depends on the temperature of the electrons heated by the prepulse. The initial diameter is chosen in a way that the scale length $L = \dfrac{n_{peak}}{\left(\frac{dn}{dr}\right)} = 2.5\mu m$ which satisfies the condition $\dfrac{4\pi c_s^2}{v_s \omega_{pi}} \ll L \leq \dfrac{\pi c}{\omega_{pi}}$ mentioned in [12]. Here r represents the radial direction of the density gradient. The density relation is thus given by,

$$n(r) = n_{peak}\left(1 - \frac{|r - r_c|}{L}\right) \tag{3.2}$$

where $r_c = 10\mu m$, $L = 2.5\mu m$ and $7.5\mu m \leq r \leq 12.5\mu m$. As the plasma has a density gradient along all the sides, the scale lengths in the laser propagation direction (Z) for the front and the rear sides $L_f = L_r = 2.5\mu m$.

In the case of a target with an increasing density profile, the laser is stopped around the relativistically corrected critical density and a significant amount of laser energy is absorbed by the electrons via collisionless absorption processes. With peak density $n_{peak} = 8n_c$, the target is transparent to the laser up to $\gamma n_c = 5.1 n_c$. The laser ponderomotive pressure pushes the electrons forward creating a charge separation region in the relativistically overdense regime. These hot electrons gain kinetic

energy and travel to the rear side of the target, perturbing the plasma in the process, and heating the entire plasma volume as a result. The laser peak hits the target at $\simeq 188fs$ and the electron momentum in the longitudinal and transverse directions are shown in Fig. 3.3(a) and 3.3(b) respectively. The time frame is considered from the instant the uniform target is hit by the pre-pulse. These phase space plots show that the electrons acquire relativistic velocities as the laser peak hits the pre-formed plasma target. The electron energy spectra at the peak of interaction ($\simeq 188fs$) [shown in Fig. 3.3(c)] gives a rough estimate of the average energy of the thermal electrons $T_h \simeq 0.76MeV$ from the slope of its linear fitting (red solid line). The temperature of the electrons further increases beyond the peak of interaction to 3.68 MeV at 225.6 fs.

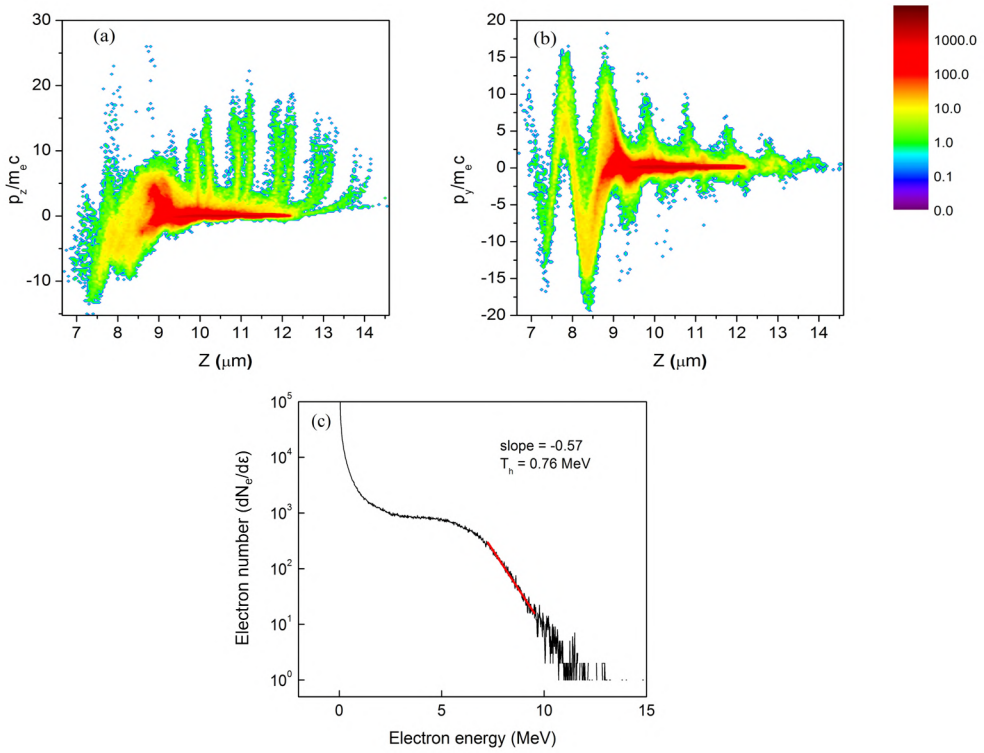

Figure 3.3: (a)The longitudinal electron momentum and (b) the transverse electron momentum along the propagation direction Z for the target with linear density gradient with $n_{peak} = 8n_c$ at time 188 fs when the laser peak intensity hits the target. The colour axis gives the particle distribution in arbitrary units. (c) is the electron energy spectrum at the same time. The red line is a linear fit for the estimation of the hot electron temperature.

Fig. 3.4 depicts the longitudinal proton momenta at three different times, (a) $t = 226fs$, (b) $t = 263fs$ and (c) $t = 338fs$ respectively. It is seen that apart from the expansion velocity (v_0) of the protons, the protons from the central peak density region attain a forward momentum [as seen in Fig. 3.4(a)]. At a somewhat later state [Fig. 3.4(b)], a shock front develops at around $Z = 11\mu m$ which evolves to a fully developed shock reflecting protons in its course at time 338 fs as seen from Fig. 3.4(c).

Apart from the classic CSA mechanism, there is a well-studied low-density variant known as Low-Density Collisionless Shock Acceleration (LDCSA) [23, 24, 25], where a combination of shock acceleration and a decreasing sheath field is present. In the presence of a decreasing density gradient in the target, the sheath electric field monotonically decreases with the distance. As a result, the ions in the high-density region experience a greater pull towards the rear-side electric field, compared to the ions in the low-density region. Accordingly, the surging of fast-moving ions in the low-density region creates an electrostatic shock front, that reflects ions in its upstream region. The upstream ions originally moving with a velocity v_0 get reflected from the shock front and attain final ion velocities $v_f = 2v_s + v_0$. These velocities, however, are greatly non-uniform as v_0 is non-uniform due to the decreasing sheath effect. In addition to that, the shock velocity v_s varies with time as the shock front travels through regions of non-uniform densities. All these effects eventually broaden the energy spectra, and the mono-energetic nature of the ions is greatly reduced.

Due to the presence of a linear density gradient in the plasma target, the inner ions experience a stronger Coulombic repulsion than the outer ions. These inner protons in the high-density zone of the plasma, as a result, move faster than the outer protons. This eventually results in the over-running of the outer protons by the inner fast-moving protons. The surging of the protons in the overtaking region excites a shock. The origin of the shock observed in the simulation may be attributed to the LDCSA mechanism as described by [25]. The time at which the inner

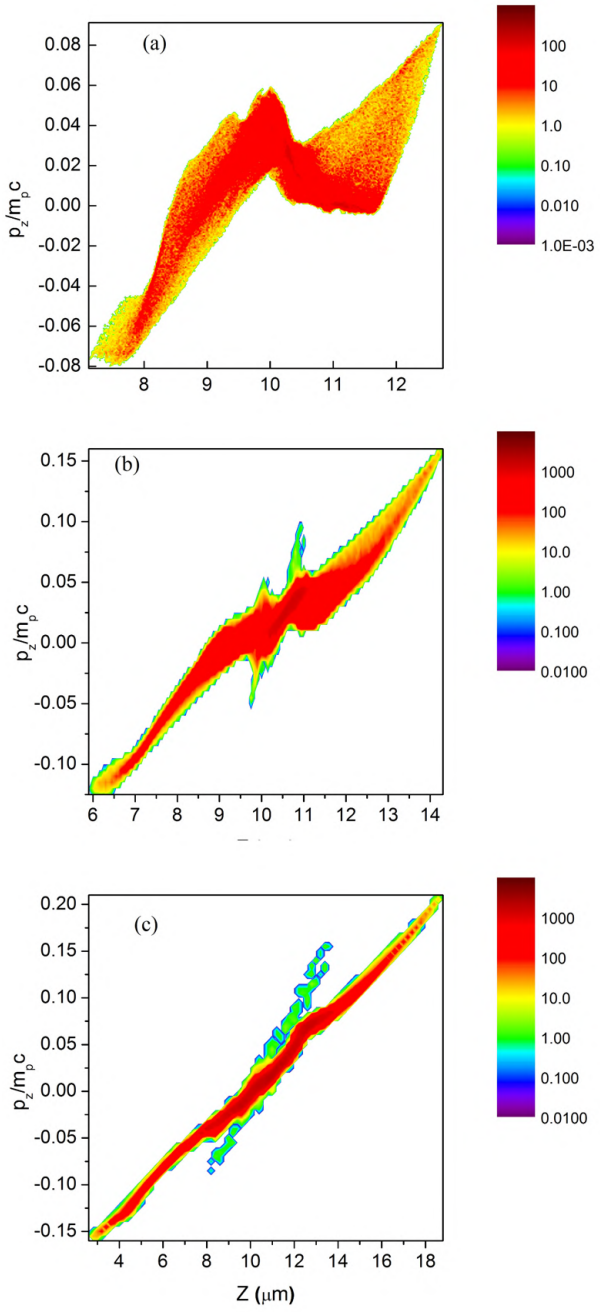

Figure 3.4: The proton longitudinal momentum and distribution at the central layer in the YZ plane along the laser axis (Z) for the target with linear density gradient and $n_{peak} = 8n_c$ at a time (a) 226 fs (before wave-breaking), (b) 263 fs (around wave-breaking time) and (c) 338 fs (after wave-breaking). The colour scheme represents the proton distribution in arbitrary units.

high-velocity protons over-take the outer low-velocity protons is termed the wave-breaking time [26]. Figures 3.4(b) and 3.4(c) are an indication that the wave breaking has caused the production of a shock and the

upstream protons are getting a further thrust along the longitudinal direction by getting reflected from the shock. The resulting velocities acquired by the reflected protons which were originally moving with v_0 velocities will thus be $v_f = 2v_s + v_0$, where v_s is the velocity of the shock. Fig. 3.4(a) and (c) give the snapshots of the proton phase spaces for times before and after wave-breaking respectively, whereas Fig. 3.4(b) shows the same around the wave breaking time. The proton density plot in Fig. 3.5(a) shows a rise in the proton density around this time ($t = 263fs$) (red curve) which gradually propagates along the positive laser direction as a shock in plasma. In the temporal evolution of the electric field [Fig. 3.5(b)], it is seen that after the initial amplified electric field driven by the radiation pressure of laser, another field appears at a later time (around 260 fs) that may be associated with the shock excited in the decreasing gradient.

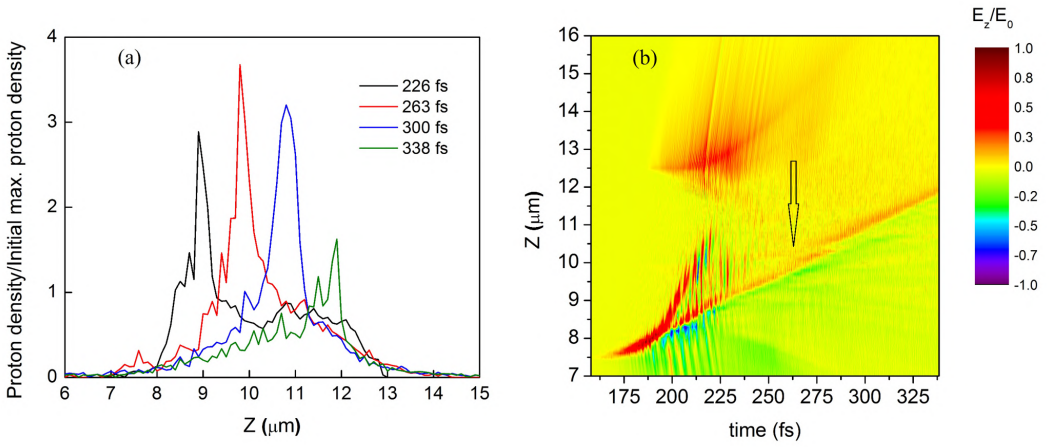

Figure 3.5: (a) The proton density along the laser axis for different times (represented by different colours) for the target with linear density gradient and $n_{peak} = 8n_c$. (b)The temporal evolution of the longitudinal electric field (normalized by the laser field E_0) for the same target. The formation of an electrostatic field due to shock is shown by an arrow.

3.3.3 Effect of peak target density

The peak density is now increased to $12n_c$ keeping L fixed. Due to the relatively steeper density gradient encountered by the laser in the target front, the laser pressure pushes a dense electron wall followed by a proton wall. The proton density in the central YZ plane plotted

against the laser axis Z [Fig. 3.6(a)] shows a high-density proton region pushed inwards by the laser pressure at time $t \simeq 230fs$. The dense proton region propagates along Z with time. This is visible in Fig. 3.6(b) where the maximum density along the laser axis attains a peak value at the centre, $Z \simeq 10\mu m$ at time $246fs$ (black curve) when the laser effect is still present. As the laser pulse dies out, the origin of the proton dynamics however shifts from a laser-pressure-based regime to an expansion regime. With the expansion of the central highly dense region of the target, its density reduces [visible in the red curve of Fig. 3.6(b)]. At 307 fs (blue curve), the maximum value of the density increases again at $Z \simeq 11\mu m$. This is similar to the previous case with peak density $8n_c$, where the expanding protons from the core eventually over-run the outer protons creating a shock in the process. In the inset of Fig. 3.6(b), the longitudinal proton phase plots are shown at times 276 fs and 307 fs. The shock reflected protons emerge from $Z \simeq 11\mu m$ at time 307 fs which were absent at time 276 fs signifying the occurrence of wave breaking between 276 fs and 307 fs. The time evolution of the longitudinal electric field plot in Fig. 3.6(c) (black square) shows a second peak emerging after the laser pulse has died off. This secondary peak is created after the wave-breaking time and is due to the excitation of the shock front. This shock front ultimately reflects the upstream protons and pushes them to high velocities. The blue circles in Fig. 3.6(c) shows the maximum velocity attained by the protons in the longitudinal direction. On the other hand, in Fig 3.6(d), we show the maximum longitudinal proton momenta of only the inner/upstream protons ($Z \geq 10\mu m$). By inner protons, we mean the protons that are accelerated in the forward Z-direction from near the centre. These protons are later reflected from the shock front generated in the decreasing density gradient of the target. It is seen from Fig. 3.6(d) that after the formation of the shock and the eventual reflection of the protons from the shock-front, the forward momentum of the upstream protons in the downward density region of the target attains an abrupt spike in its value. This effect at $t > 280fs$ further indicates

the occurrence of the wave-breaking. The reflection of the protons in the path of the shock is responsible for an increase in the final proton energy. The blue circles in Fig. 3.6(c) showing the maximum longitudinal velocity attained by the protons increases steadily up to a certain time (wave breaking time), thereafter it varies proportionally to $ln(0.858\omega_{pi}t)$ [26]. To study the effect of the central peak density on

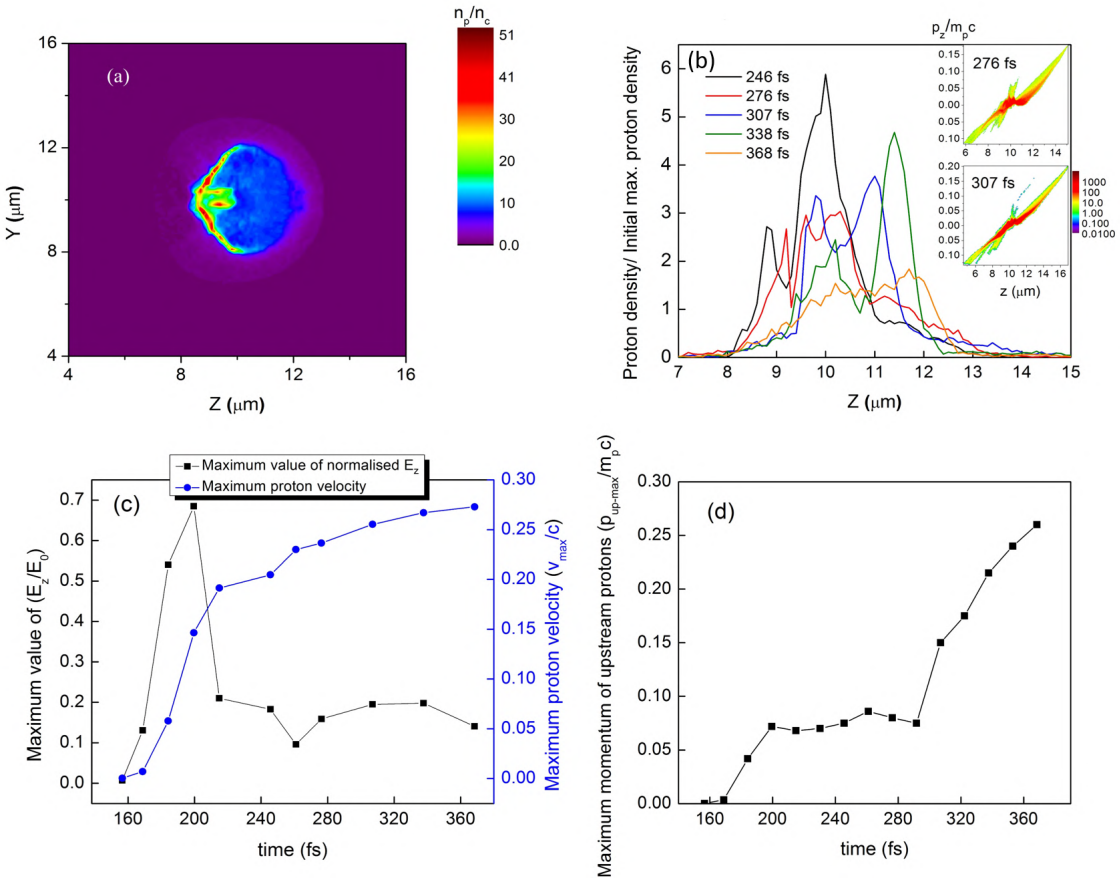

Figure 3.6: (a) The proton density plot in the central YZ plane for the target with linear density gradient and peak density $n_{peak} = 12n_c$ at time $\approx 230fs$. The laser radiation pressure pushes the protons from the target front-side creating a high-density proton front. (b) is the proton density along the central laser axis for different times (represented by different colours). The inset figures show the longitudinal proton momenta along Z at times 276 fs and 307 fs. For the same target, the time evolution is shown for (c) the longitudinal electric field (black squares) and the maximum proton velocity (blue circles), and (d) the maximum longitudinal momentum of the upstream protons (from the core region) at the central layer in the YZ plane. In the blue curve (circles) of Fig. 4(c) the maximum value of the proton velocity for a particular time among all the protons (including the sheath accelerated protons) are plotted against time, whereas in Fig. 4(d) the maximum longitudinal momenta of only the upstream ions are plotted against time.

the dynamics of the accelerated protons, a comparison is made between

three targets having peak densities $n_{peak} = 8n_c$, $12n_c$, and $15n_c$. The longitudinal electric field and the corresponding proton momentum plot of the three targets show the onset of the proton reflection from the shock front at $\simeq 300fs$ [Fig. 3.7(a-b)] and at a later time $\simeq 338fs$ in Fig. 3.7(c-d). In Fig. 3.7(a), the central peak is pronounced in the case of $n_{peak} = 12n_c$ that helps in the reflection of protons from the shock front. With a large number of shock reflected protons, the energy achieved by the protons reaches an optimum value in the case with $n_{peak} = 12n_c$. As the density is further increased to $n_{peak} = 15n_c$, the absorption efficiency decreases as the laser encounters a steep gradient. This effect restrains volumetric heating of the plasma which restricts the shock formation in this case. Due to the rise in the density gradient for the target with $n_{peak} = 15n_c$ the target front side behaves almost like a sharp vacuum-plasma interface. The radiation pressure effect plays a dominant role in this case to accelerate the protons.
The 1D simulation study by Weng, et al [27] with extremely high laser intensities ($a_0 = 100$) obtained a boundary density of $12n_c$ which separates the effect of an incomplete hole-boring from a classical hole-boring case. It is worth mentioning that, for the linear density cases in the present work, an optimum value of peak density is attained at $12n_c$. The targets used in the present simulations, however, are of non-uniform densities. Consequently, the mechanism underlying the production of energetic protons in our case is different from those obtained in [27]. Besides, we can see that the occurrence of the shock takes place at a much later time at the decreasing density region of the target which indicates that the source of the shock is not laser-based. Instead, it is the over-running of the outer ions by the inner fast-moving ions that cause the shock in our cases.

Due to the non-uniformity in the density, the target heating is non-uniform, as a result, the protons attain non-uniform velocities $v_f = 2v_s + v_0$ towards the sheath field. Moreover, the propagation of the shock down the density gradient results in a steadily-varying shock velocity. These

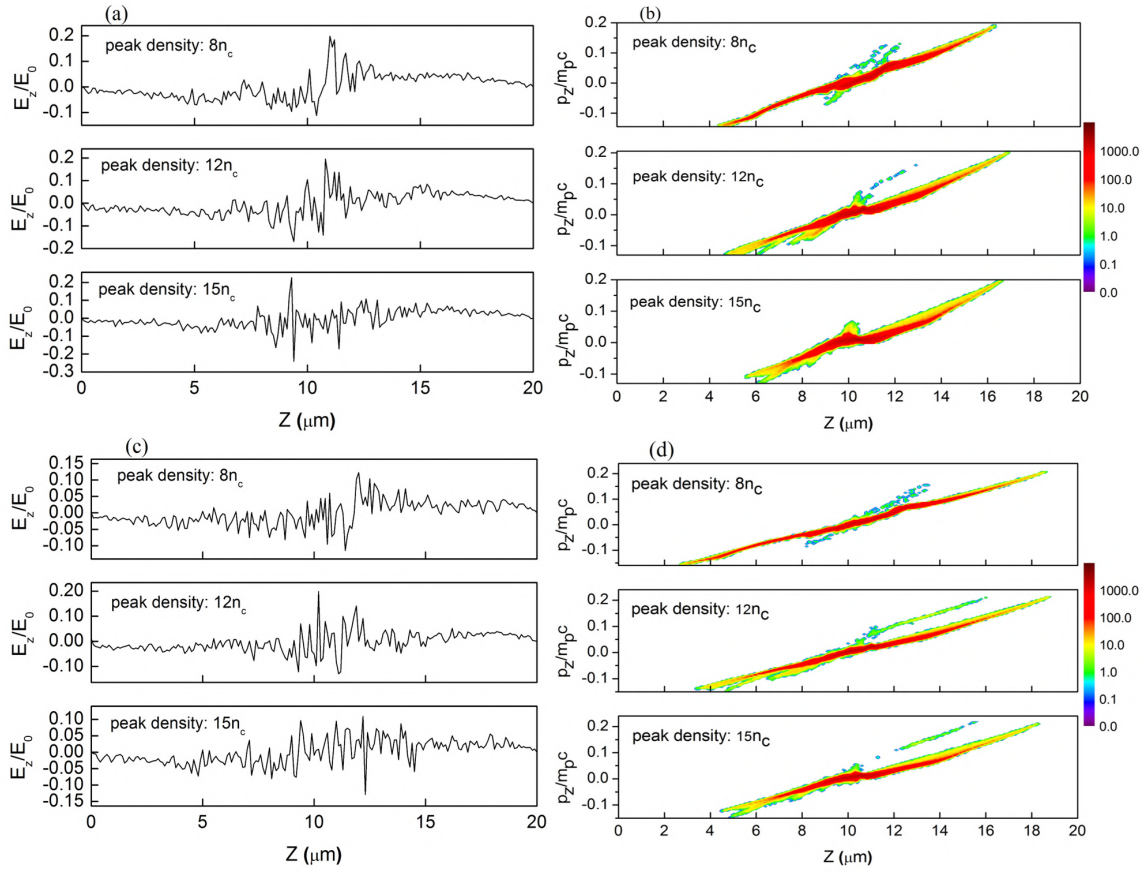

Figure 3.7: The longitudinal electric field in the central YZ plane at (a)300 fs and (c) 338 fs; and the longitudinal proton momentum along Z at (b)300 fs and (d)338 fs for three different peak target densities. The colour axis in (b) and (d) represents the proton distribution in arbitrary units. The presence of a strong peak in the case with $n_{peak} = 12n_c$ in (c) leads to a higher number of protons obtaining momentum from near the centre in the corresponding phase plot in (d).

effects add up to the total energy of the protons and as a consequence, the proton energy spectra broaden significantly (as seen in Fig. 3.8). The highest energetic protons are thus affiliated to the combined effect of shock acceleration, TNSA, and plasma expansion.

3.3.4 Radially Gaussian density distribution

In this section, we study the role of Gaussian inhomogeneity type on the acceleration of protons, and therefore, the density profile is changed from a linear gradient to a Gaussian-shaped one with the peak density located at the centre of the plasma sphere, and the density radially dropping towards the sides following a Gaussian shape. The density equation

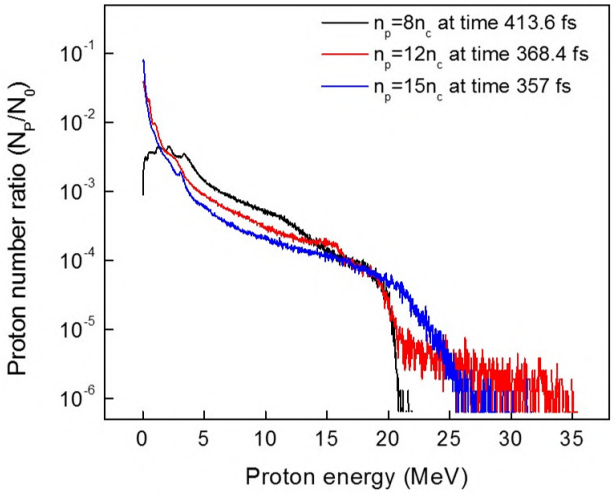

Figure 3.8: The proton energy spectra comparing different peak densities having a linear density gradient starting from the target centre at their respective saturation times.

thus becomes,

$$n(r) = n_{peak} exp\left[-\frac{1}{2}\left(\frac{r}{b}\right)^2\right] \tag{3.3}$$

where, r is the distance from the centre, and $b \approx 0.425\times$ FWHM. As $r \to \infty$, $n(r) \to 0$, but for practical purposes and comparison with the linear density profile, $n(r) \to 0$ as $r \to 4\mu m$. This length is chosen in a way that makes the inhomogeneity FWHM $\sim 2.5\mu m$ which is comparable to the scale length of the linear cases.

We consider a plasma sphere with peak density $n_{peak} = 15n_c$. Due to the steep density gradient at the front side, the laser quickly encounters a relativistically overdense regime. The laser pressure pushes the plasma inwards creating a density spike that is seen to form around $Z = 9.3\mu m$ marking [Fig. 3.9 (a)] at $t \approx 220fs$. This curve-shaped proton dense region travels along Z with a velocity $0.057c$. Fig. 3.9(a) shows that the radiation pressure effect of the laser pulse could be felt beyond the relativistically critical density surface $Z = 8.6\mu m$ (where $n_{peak} \simeq 5.1n_c$). The accumulation of the protons ahead of the laser pulse is observed at $Z = 8.75\mu m$. Here, the initial plasma density is $n_{peak} \simeq 6.85n_c$. Feeding this value in the expression for hole-boring velocity, we get, $v_{hb} \simeq 0.059c$. This value is close to the velocity of the dense concave region $\approx 0.057c$ thus confirming that this propagating dense region originated near the

front side of the target is created due to the hole-boring mechanism of the laser. This propagating high-density region, at later times, starts reflecting protons in its upstream region and these reflected protons can be seen in Fig. 3.9(b) (at 275 fs) as a dense bunch moving ahead of the high-density concave surface. The velocity of this propagating proton-dense bunch is found to be $0.106c$. The corresponding longitudinal momentum plots [Fig. 3.9(c-d)] shows protons getting predominantly accelerated from the front side of the target. It is seen from Fig 3.10(a)

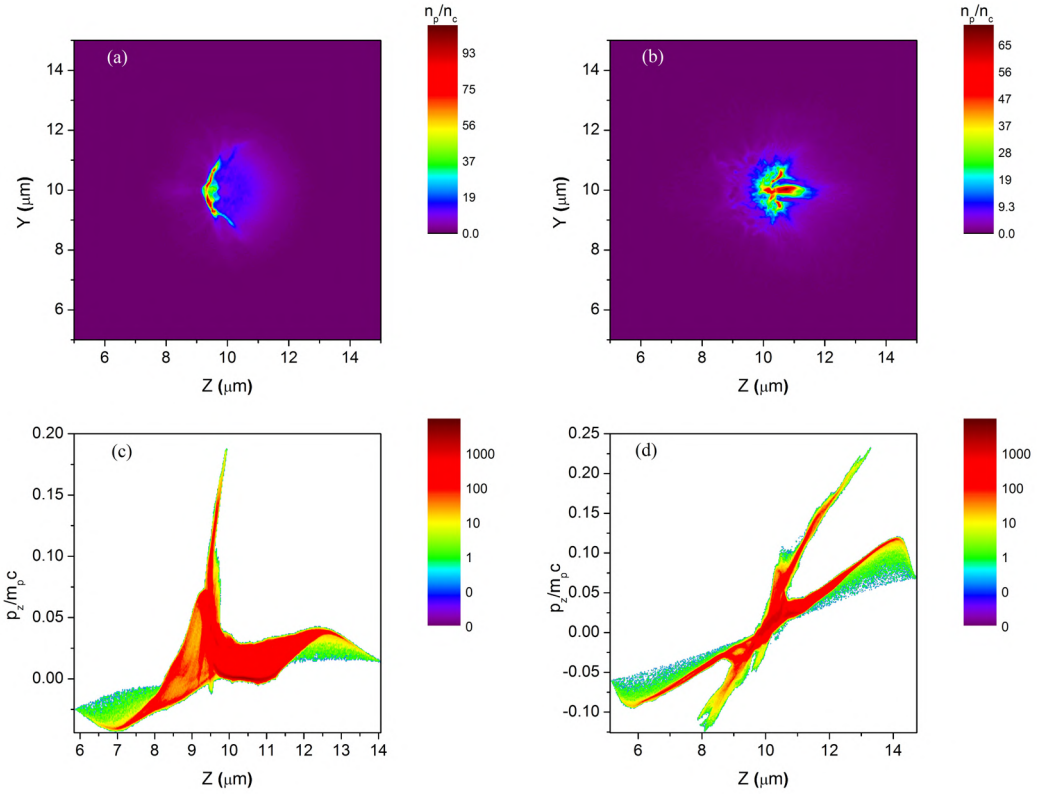

Figure 3.9: For the target with Gaussian density profile and peak density $n_{peak} = 15n_c$, the proton density in the central YZ plane at (a)220 fs and (b) 275 fs; and the longitudinal proton momentum along Z at (c)220 fs and (d)275 fs. The colour axis represents proton numbers in arbitrary units.

that the divergence angle of the emitted energetic proton beam is $\simeq 15$ degrees which suggests that the emitted beam is considerably collimated. As the collimated proton bunch propagates beyond the central peak density region of the plasma, it comes across a non-uniform plasma density due to the density ramp at the target rear. This is the reason behind the broadening of the proton spectra at the high-energy end. The quasi-

monoenergetic structures formed in the proton spectra at different times in Fig. 3.10(b) are due to the fairly constant velocities with which the protons travel after getting reflected from the high-density region, before getting pulled to non-uniform velocities by the sheath field at the rear surface of the target. The protons from the central portion of the target are responsible for the appearance of these quasi mono-energetic peaks in the energy spectra. It is observed in Fig. 3.10(c) that the energy scaling law with intensity follows that of the hole boring mechanism: $\varepsilon \sim I_L$ [28] for the intensity range considered in our simulations.

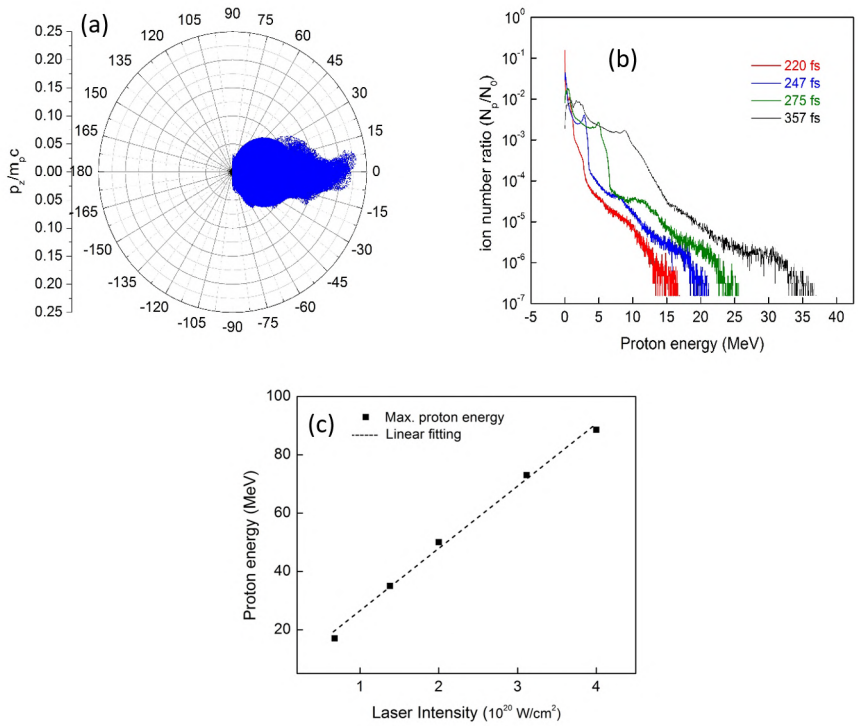

Figure 3.10: For the target in Fig. 3.9, (a) shows the divergence of the protons (in degrees) at 275 fs. (b) is the proton energy spectra at different times represented by different colours. (c) Scaling of maximum proton energy obtained using the same target with different peak laser intensities shows a linear variation inferring the association of the hole boring RPA. The dotted line is the linear fit for the simulated values.

3.3.5 Influence of density inhomogeneity

To study the effect of introducing a density gradient in the plasma target, we present a comparison of the results using such targets with a

uniform density plasma sphere. In our cases, the density inhomogeneity gradually increases from the sides to reach a peak value at the centre. As the laser is incident on the front side of the target, a gradually increasing density profile facilitates a stronger energy conversion from the laser to the electrons (see Fig. 3.12(a)). A high absorption efficiency later on translates to higher proton energies. On the other hand, the use of uniform overdense targets cause a major portion of the laser energy to get reflected.

The presence of a decreasing density profile at the rear side has a crit-

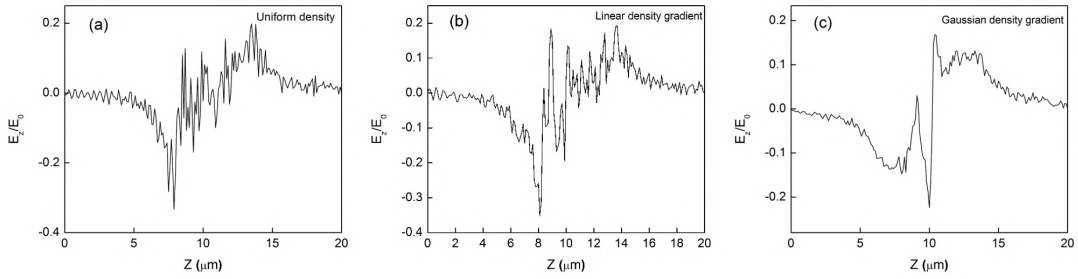

Figure 3.11: The longitudinal electric field in the central YZ plane along Z for (a) the uniform density target with density $12n_c$, (b)target with linear density gradient and (c) target with Gaussian density gradient with $n_{peak} = 12n_c$ at time 245.6 fs.

ical role in decreasing the energy spread of the mono-energetic protons in the energy spectra at the later stages of acceleration. Fig. 3.11(a-c) compares the longitudinal electric field between the targets having a density inhomogeneity with a uniform density target having density $12n_c$. The uniform target is a sphere of diameter $5\mu m$ which is equal to the inhomogeneity scale length used in the simulations for the density gradients. The number of particles considered for the simulation of the uniform target is also kept equal to the inhomogeneous cases. It is seen that the TNSA field at the rear end of the target ($Z \sim 14\mu m$) is reduced in the case of Gaussian targets. In presence of an initial exponential scale length, the amplitude of the sheath electric field at early stages (before wave breaking) is given by $E_{TNSA} = \dfrac{K_B T_h}{eb}$ [26]. This may be the reason for the reduction in the TNSA field in comparison to a uniform plasma target observed in our simulation. Figure 3.11(c) shows that in

the case of the Gaussian target the sheath field is characterised by a uniform plateau, which is not seen in Figs. 3.11(a) and (b). This uniform field accelerates protons to uniform velocities v_0 (as seen in Fig. 3.10(c)), limiting the effects of the TNSA field on the protons reflected by the hole-boring at early times. As a consequence, the energy spread of the protons reflected by the hole-boring is reduced.

The electron energies achieved using three different target densities are shown in Fig. 3.12(a). The target with uniform density, i.e. with abrupt vacuum-plasma interface showed the lowest laser-to-electron energy conversion. This is consistent with the previous literature which suggests pre-plasma for an increased laser energy absorption [5, 6, 7, 8]. It is observed from Fig. 3.12(a) that the linear density inhomogeneity has the highest values of electron energy inferring an enhanced target heating which supports the formation of shocks in later times. The shock accelerated protons seen in Fig. 3.7(b) and (d) arise due to the higher electron energy achieved, which heats the target efficiently. In the case of the target with Gaussian inhomogeneity, the steepness of the density gradient on the front side is more, compared to the linear inhomogeneity. As a result absorption of laser energy gets reduced thus facilitating the hole-boring effect to play its role rather than the LDCSA mechanism. The blue curve in Fig. 3.12(a) signifies intermediate electron energy in the Gaussian case supporting a reduced target heating. A strong RPA-HB was the factor behind the desirable feature of mono-energetic protons in the energy spectra at around 5 MeV [Fig. 3.12(b) (blue curve)]. In addition to this, a comparatively fast-dropping density at the rear side made the sheath field contribution in the low-density region quite negligible [comparing Fig. 3.12(c) and (d)]. As the proton front pushes most of the protons ahead of it to high energies, the broadening of the spectra due to the weak sheath field becomes limited. This may be the reason behind a sharper mono-energetic peak of protons in the case of a Gaussian density gradient, compared to a linear one.

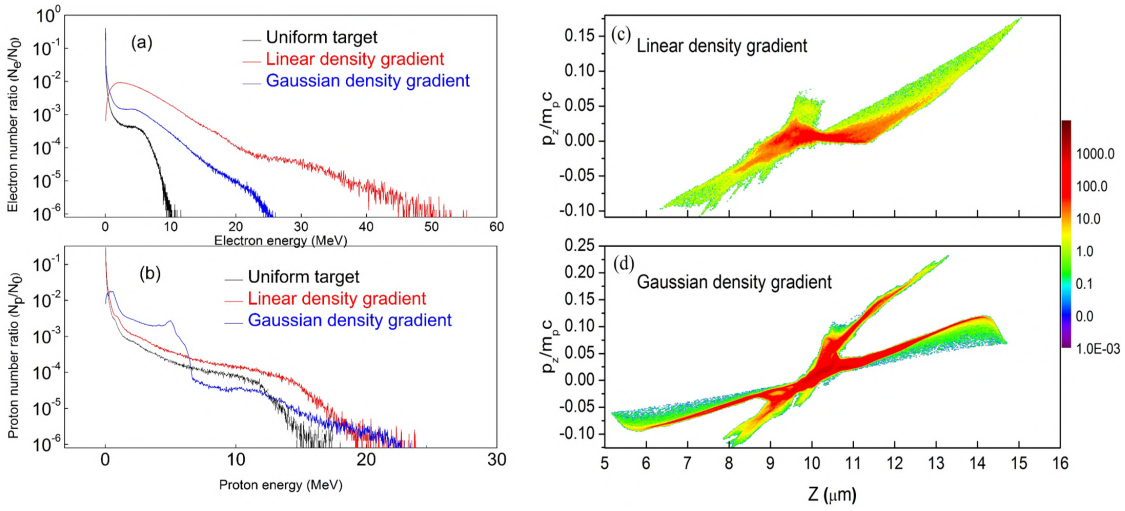

Figure 3.12: (a) The comparison between the electron energies at $190fs$ for three different density types: a uniform density target (black), target with a linear density gradient (red), and target with Gaussian density gradient (blue). The linear gradient shows the highest electron energies. (b) The comparison between proton energies at time 275 fs for $n_{peak} = 15n_c$ for the three different density profiles. The longitudinal proton momentum and distribution for $n_{peak} = 15n_c$ at time 275 fs for (c)the linear case and (d) the Gaussian case. The colour axis represents protons in arbitrary units. The laser intensity is $I_L = 1.37 \times 10^{20} Wcm^{-2}$.

3.4 Conclusion

In this chapter, we have studied the interaction mechanisms involved in the irradiation of a circularly polarized, ultra-short, intense laser with a micron-sized hydrogen sphere having a density profile radially decreasing starting at the target centre. The laser facilities around the globe produce a pre-pulse which creates a smooth density gradient inside the target. The density profile can be tailored by tuning the target density and delay between the pre-pulses and the main pulse. The comparison of different density profiles in a spherical target having dimensions of the order of the laser spot size, when heated with a pulsed femtosecond laser is observed using 3D PIC simulation. The proton beams are accelerated from the interaction region with the involvement of a collection of acceleration mechanisms. It is observed that the target parameters contribute collectively to generate an energetic jet of protons. The results of the reported work can be summed up in the following points:

1. The effect of various pre-pulse strengths has been studied and found

that the presence of the pre-pulse (or the density gradient) helps in increasing the energy of the protons.

2. The dominant acceleration process depends on the density gradient (or the peak density at the centre). An optimum value of peak density $12n_c$ is obtained for the linear density profile where the protons are accelerated due to the interplay of radiation pressure and LDCSA with a further contribution from the sheath electrostatic field. This optimum case of peak density is observed for the target providing intermediate opacity to the laser. The introduction of a density gradient at the target front side resulted in an increased absorption which in turn enhanced the proton energy.

3. The effect of a novel Gaussian-shaped inhomogeneity on the proton acceleration is analysed and found that the sheath contribution is weaker for this profile, compared to a linear one. The increased density gradient in the front side of the Gaussian density target facilitates the hole-boring mechanism of the laser which accelerates the protons from the front side with a near-uniform velocity. For the target with density $15n_c$ the presence of a Gaussian-shaped density gradient increases the maximum proton energy from $15MeV$ (in the uniform density case) to $35MeV$ using a laser of peak intensity $I_L = 1.37 \times 10^{20} Wcm^{-2}$. It is seen that instead of a sharp TNSA field at the rear surface, which is a characteristic of a uniform target, a decaying field is formed at the expanding rear surface of the target. The retention of the mono-energetic peak in the proton spectra poses an advantage of using such targets over uniform density targets.

4. The maximum energy obtained using a Gaussian profile is almost equal to that of the linear profile; however, the mono-energetic feature of the protons is greatly enhanced in the Gaussian-shaped density profile. The proton energy scales as $\varepsilon \propto I_L$ for the Gaussian case which is a signature of the hole-boring RPA mechanism.

Thus, it is found that the proton beam properties may be tuned as

per the requirements by engineering novel density profiles in the targets. By changing the density features of the target the proton beam characteristics can be controlled accordingly. A Gaussian-shaped inhomogeneity showed a promising ground for future studies on ion beam dynamics. Using further refinement, the present study may be used to experimentally cultivate energetic protons.

Bibliography

[1] Schwoerer, H., Pfotenhauer, S., Jäckel, O., Amthor, K.-U., Liesfeld, B., Ziegler, W., Sauerbrey, R., Ledingham, K., and Esirkepov, T. Laser-plasma acceleration of quasi-monoenergetic protons from microstructured targets. *Nature*, 439(7075):445, 2006.

[2] Hegelich, B. M., Albright, B., Cobble, J., Flippo, K., Letzring, S., Paffett, M., Ruhl, H., Schreiber, J., Schulze, R., and Fernández, J. Laser acceleration of quasi-monoenergetic mev ion beams. *Nature*, 439(7075):441–444, 2006.

[3] Cialfi, L., Fedeli, L., and Passoni, M. Electron heating in subpicosecond laser interaction with overdense and near-critical plasmas. *Phys. Rev. E*, 94(5):053201, 2016.

[4] Sgattoni, A., Londrillo, P., Macchi, A., and Passoni, M. Laser ion acceleration using a solid target coupled with a low-density layer. *Phys. Rev. E*, 85(3):036405, 2012.

[5] Sentoku, Y., Bychenkov, V. Y., Flippo, K., Maksimchuk, A., Mima, K., Mourou, G., Sheng, Z., and Umstadter, D. High-energy ion generation in interaction. of short laser pulse with high-density plasma. *Appl. Phys. B*, 74(3):207–215, 2002.

[6] Kluge, T., Enghardt, W., Kraft, S., Schramm, U., Zeil, K., Cowan, T., and Bussmann, M. Enhanced laser ion acceleration from mass-limited foils. *Phys. Plasmas*, 17(12):123103, 2010.

[7] Andreev, A., Okada, T., and Toraya, S. Ultra-intense laser pulse absorption and fast particles generation at interaction with inhomogeneous foil target. In *AIP Conf. Proc.*, volume 634, 303–310. American Institute of Physics, 2002.

[8] Andreev, A., Platonov, K. Y., Okada, T., and Toraya, S. Nonlinear absorption of a short intense laser pulse in a nonuniform plasma. *Phys. Plasmas*, 10(1):220–226, 2003.

[9] Andreev, A., Sonobe, R., Kawata, S., Miyazaki, S., Sakai, K., Miyauchi, K., Kikuchi, T., Platonov, K., and Nemoto, K. Effect of a laser prepulse on fast ion generation in the interaction of ultrashort intense laser pulses with a limited-mass foil target. *Plasma Phys. Control. Fusion*, 48(11):1605, 2006.

[10] Fiúza, F., Stockem, A., Boella, E., Fonseca, R., Silva, L., Haberberger, D., Tochitsky, S., Gong, C., Mori, W. B., and Joshi, C. Laser-driven shock acceleration of monoenergetic ion beams. *Phys. Rev. Lett.*, 109(21):215001, 2012.

[11] Feng-Chao, W. Effects of density profile and multi-species target on laser-heated thermal-pressure-driven shock wave acceleration. *Chin. Phys. B*, 22(12):124102, 2013.

[12] Boella, E., Fiúza, F., Novo, A. S., Fonseca, R., and Silva, L. Ion acceleration in electrostatic collisionless shock: on the optimal density profile for quasi-monoenergetic beams. *Plasma Phys. Control. Fusion*, 60(3):035010, 2018.

[13] Novo, A. S., Kaluza, M., Fonseca, R., and Silva, L. Optimizing laser-driven proton acceleration from overdense targets. *Sci. Rep.*, 6:29402, 2016.

[14] Svedung Wettervik, B., DuBois, T., and Fülöp, T. Vlasov modelling of laser-driven collisionless shock acceleration of protons. *Phys. Plasmas*, 23(5):053103, 2016.

[15] Yang, Y., Zhou, C., Huang, T., He, M., Wu, S., Cai, T., Qiao, B., Yu, M., Ruan, S., and He, X.-t. Manipulating laser-driven proton acceleration with tailored target density profile. *Plasma Phys. Control. Fusion*, 2020.

[16] Pšikal, J., Limpouch, J., Kawata, S., and Andreev, A. Pic simulations of femtosecond interactions with mass-limited targets. *Czech. J. Phys.*, 56(2):B515–B521, 2006.

[17] Ostermayr, T. M., Haffa, D., Hilz, P., Pauw, V., Allinger, K., Bamberg, K.-U., Böhl, P., Bömer, C., Bolton, P., Deutschmann, F., et al. Proton acceleration by irradiation of isolated spheres with an intense laser pulse. *Phys. Rev. E*, 94(3):033208, 2016.

[18] Hilz, P., Ostermayr, T., Huebl, A., Bagnoud, V., Borm, B., Bussmann, M., Gallei, M., Gebhard, J., Haffa, D., Hartmann, J., et al. Isolated proton bunch acceleration by a petawatt laser pulse. *Nat. Commun.*, 9(1):1–9, 2018.

[19] Lecz, Z. and Andreev, A. Shock wave acceleration of protons in inhomogeneous plasma interacting with ultrashort intense laser pulses. *Phys. Plasmas*, 22(4):043103, 2015.

[20] Weng, S., Sheng, Z., Murakami, M., Chen, M., Liu, M., Wang, H., Yuan, T., and Zhang, J. Optimization of hole-boring radiation pressure acceleration of ion beams for fusion ignition. *MRE*, 3(1):28–39, 2018.

[21] Bhagawati, A., Kuri, D. K., and Das, N. Proton acceleration due to laser plasma interactions from mass-limited spherical targets. *Phys. Plasmas*, 26(9):093106, 2019.

[22] Upadhyay, A., Patel, K., Rao, B., Naik, P., and Gupta, P. Three-dimensional simulation of laser–plasma-based electron acceleration. *Pramana*, 78(4):613–623, 2012.

[23] d'Humières, E., Antici, P., Glesser, M., Boeker, J., Cardelli, F., Chen, S., Feugeas, J., Filippi, F., Gauthier, M., Levy, A., et al.

Investigation of laser ion acceleration in low-density targets using exploded foils. *Plasma Phys. Control. Fusion*, 55(12):124025, 2013.

[24] Gauthier, M., Levy, A., d'Humieres, E., Glesser, M., Albertazzi, B., Beaucourt, C., Breil, J., Chen, S., Dervieux, V., Feugeas, J., et al. Investigation of longitudinal proton acceleration in exploded targets irradiated by intense short-pulse laser. *Phys. Plasmas*, 21(1):013102, 2014.

[25] Antici, P., Boella, E., Chen, S., Andrews, D., Barberio, M., Böker, J., Cardelli, F., Feugeas, J., Glesser, M., Nicolaï, P., et al. Acceleration of collimated 45 mev protons by collisionless shocks driven in low-density, large-scale gradient plasmas by a 10 20 w/cm 2, 1 μm laser. *Sci. Rep.*, 7(1):1–9, 2017.

[26] Grismayer, T. and Mora, P. Influence of a finite initial ion density gradient on plasma expansion into a vacuum. *Phys. Plasmas*, 13(3):032103, 2006.

[27] Weng, S., Murakami, M., Mulser, P., and Sheng, Z. Ultra-intense laser pulse propagation in plasmas: from classic hole-boring to incomplete hole-boring with relativistic transparency. *New J. Phys.*, 14(6):063026, 2012.

[28] Macchi, A. *A Superintense Laser-Plasma Interaction Theory Primer*. Springer Science & Business Media, 2013.